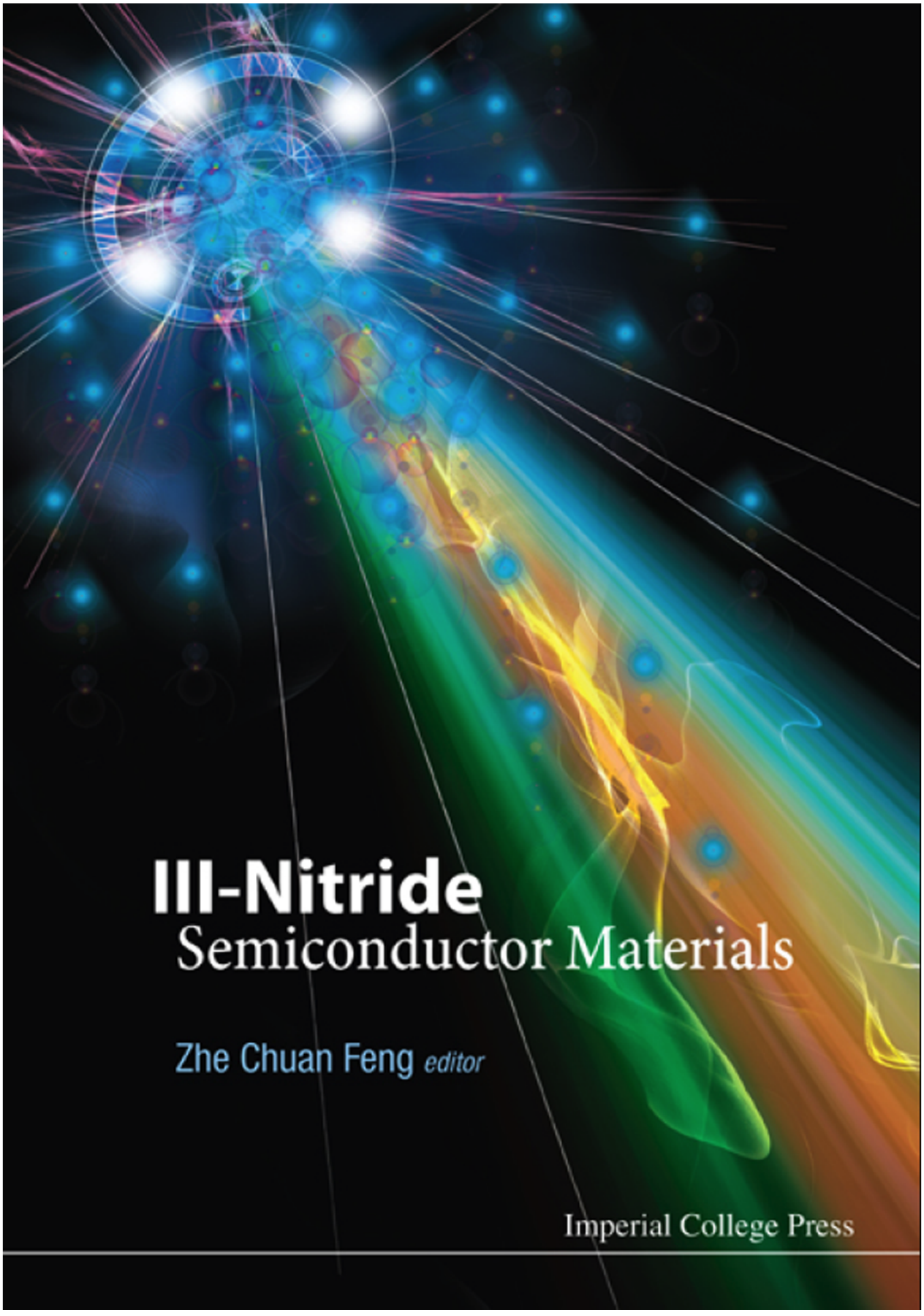
III-Nitride
Semiconductor Materials
Zhe Chuan Feng editor
Imperial College Press

III-Nitride
Semiconductor Materials

III-Nitride semiconductor materials — (Al, In, Ga)N — are excellent wide band gap semiconductors very suitable for modern electronic and optoelectronic applications. Remarkable breakthroughs have been achieved recently, and current knowledge and data published have to be modified and upgraded. This book presents the new developments and achievements in the field.

Written by renowned experts, the review chapters in this book cover the most important topics and achievements in recent years, discuss progress made by different groups, and suggest future directions. Each chapter also describes the basis of theory or experiment.

The III-Nitride-based industry is building up and new economic developments from these materials are promising. It is expected that III-Nitride-based LEDs may replace traditional light bulbs to realize a revolution in lighting. This book is a valuable source of information for engineers, scientists and students working towards such goals.

Key Features

- Provides useful information to material growers and evaluators, device design and processing engineers
- Covers recent developments in III-Nitride semiconductors materials
- Predicts future directions for further research and development

P437 hc

ISBN 1-86094-636-4

Imperial College Press

www.icpress.co.uk

CHAPTER 6

INDIUM-NITRIDE GROWTH BY HIGH-PRESSURE CVD: REAL-TIME AND EX-SITU CHARACTERIZATION

Nikolaus Dietz

Department of Physics & Astronomy, Georgia State University
P.O. Box 4106, Atlanta GA 30302-4106, USA
E-mail: ndietz@gsu.edu

Growth techniques that employ elevated pressures offer a pathway to overcome limitations in the epitaxy of high quality indium-rich group III-nitride compounds and related materials, which exhibit large thermal decomposition pressures. High-pressure chemical vapor deposition (HPCVD) opens an avenue for controlling stoichiometric single-phase surface compositions at optimal processing temperatures. The application of real-time optical monitoring techniques such as ultraviolet absorption spectroscopy (UVAS), principal angle reflectance spectroscopy (PARS) and laser light scattering (LLS) are crucial to gain insights into the gas-phase and surface chemistry during the heteroepitaxial nucleation and growth process. They are also critical for controlling the chemical vapor deposition process, which allows for the formation of heteroepitaxial layers of improved perfection with respect to stoichiometry, the elimination of extended defects, and the chemical integrity of the interface. The real-time optical monitoring techniques employed during InN growth demonstrated their utility in the optimization and engineering of the growth process, as well as providing crucial insights in gas phase decomposition dynamics and in surface chemistry processes under HPCVD conditions. The optical InN layer analysis by absorption spectroscopy shows that the shift of the absorption edge from 1.85eV down below 0.63eV is caused by a series of absorption centers, appearing as the stoichiometry ratio of indium and nitrogen is varied. This coincides with a sharpening of the Raman modes, indicating an improved crystalline structure.

1. Introduction

The fabrication of emerging detector and emitter structures as well as high-frequency/high-power devices operating at high temperature(s) that are based on group III-nitride compound alloys have attracted much interest in recent years. This is due to their wide range of applications that cannot be accomplished with present Si and group III-P/As materials technology. Of particular interest is an improved knowledge of the binary base system InN, and to which extend alloys and heterostructures can be formed for fabrication of optical electronic device structures.[1,2] GaN and AlN alloys and heterostructures are the most studied group III-nitride compounds, however, InN is becoming increasing more significant due to its unique optoelectronic properties.

At present, the growth of III-nitrides is mostly performed using low-pressure deposition techniques such as molecular beam epitaxy (MBE),[3-5] organometallic chemical vapor deposition (MOCVD - also denoted as MOVPE)[6,7] or variations of both. However, low-pressure deposition processes are limited to regimes where the partial pressures of the constituents do not differ vastly and the decomposition process can be countered by off-equilibrium processing conditions. The application of these techniques for the growth of InN and related indium rich III-N alloys becomes a major challenge due to their stoichiometric instabilities and low dissociation temperatures, leading to inconsistent and process dependent materials properties. Even for the binary InN compound itself many of the fundamental properties are still debated. The considerable uncertainty over the band gap of InN,[2,3,8,9] the influence of the intrinsic materials point defect chemistry on the optical and electrical properties,[1] and the effect of extrinsic impurities such oxygen on the band gap,[10,11] show a decided lack of understanding of this system. Controversial reviews of the present status of InN growth and characterization have been provided by Bhuiyan et.al.[1] and Davydov et.al.[12] These reviews imply that new approaches for the growth of In-rich group-III-nitride alloys need to be explored in order to improve the structural and optical properties of InN and related alloys.

CVD growth of InN requires low growth temperature to overcome thermal decomposition pressures, thus limiting the quality of InN and

related group III-nitride epilayers.[1,13-15] This low growth temperature requires the application of extremely high V-III ratios in order to prevent the formation of metal droplets on the surface. Studies on the decomposition of InN layers[10] have shown that oxygen is easily incorporated into the InN crystal under thermal treatments, and has been suggested as the source for the wide discrepancy in reports in the bandgap energy of InN. Recent studies of the indium - nitrogen system[16] show considerable uncertainty in the p-T-x relations due to missing experimental validation. However, studies of the nitrogen pressure needed to prevent thermal decomposition of bulk InN provided a relationship given by[17]

$$p(N_2) \rightarrow p_0 \exp\left[-\frac{\Delta H_r}{R}\left(\frac{1}{T} - \frac{1}{T_0}\right)\right], \quad (1)$$

which results in the $p\text{-}T^{-1}$ relation shown in Fig.1,[17] where ΔH_r represent the heat of formation, R the universal gas constant and T the equilibrium temperature. This relation indicates that in the pressure range $p_{N_2} \leq 10^2$ bar and for substrate temperatures ≤ 900K the surface decomposition of InN will be effectively suppressed.

Thin film growth at high pressures requires – in addition to specific reactor design considerations – careful considerations towards flow kinetics, gas phase reactions, and the diffusion through the surface boundary layer as well as altered surface chemistry.[18] To minimize gas phase reactions, extract sufficient organometallic (OM) nutrients from the bubbler, and embed the precursor flow in the main reactor gas stream, a pulsed precursor injection scheme has been implemented, which is essential for

- compression of precursors to reactor pressure,
- minimization of gas phase reactions,
- engineered nucleation kinetics and layer growth, and
- analyzing the gas-phase and surface decomposition dynamics in real-time.

The remainder of the article is sections as follows. Section II provides a brief summary on the HPCVD reactor characteristics. The following sections provide results on the topics as listed:

2. HPCVD Reactor characteristics;
3. Reactor flow characterization;
4. Optical characterization of the precursors ammonia and TMI;
5. Flow kinetics: Analysis utilizing pulsed gas injection;
6. Precursor decomposition dynamics at higher pressures;
7. Growth of InN: Real-time optical monitoring;
8. Ex-situ characterization of InN layers, and
9. Summary and Outlook.

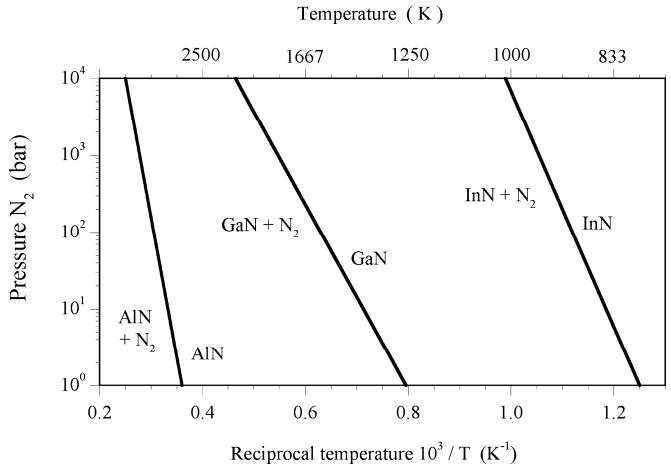

Fig. 1. Thermal decomposition pressure vs. reciprocal temperature for AlN, GaN and InN.[17]

2. HPCVD Reactor Characteristics

In order to explore the growth at higher pressures, a high-pressure flow channel reactor with incorporated real time optical characterization capabilities[19-21] was implemented at Georgia State University, GSU, capable of growing group III-nitrides at reactor pressures up to 100 bar. The implementation of the HPCVD system is schematically depicted in Fig.2, which shows the reactor cross section containing the substrates and optical monitoring plane, perpendicular to the flow direction. The flow channel is embedded in an inner reactor cylinder, while an outer reactor pressure vessel confines the overall pressure for well above 100

bar. The substrates are symmetrically embedded in the upper and lower part of the flow channel in order to prevent preferential material deposition. A fully machined and assembled half-part of the inner reactor system is shown in Fig.3.

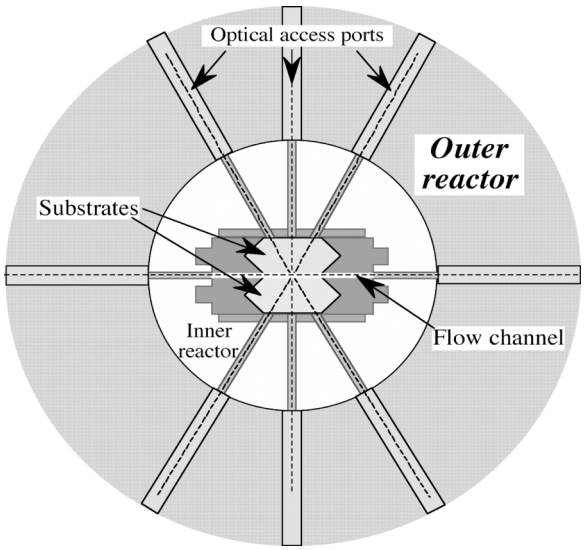

Fig. 2. Schematic cross section of the reactor containing the optical access ports and the center of the substrates. Two optical ports provide access to the flow channel and three ports in each of the two half sections of the reactor provide access to the growth surface.

Two of these inner parts together form the inner shell of the HPCVD reactor, which are inserted into the outer pressure confinement shell. Optical access ports are integrated along the center axis of the substrates allowing optical characterization of flow kinetics, gas phase reactions via LLS and UVAS. Optical access ports also provide for access to the substrate surface through the backside, enabling the use of principal angle reflectance spectroscopy (PARS) and LLS in back-scattering geometry.[19,22,23] Both half parts of the inner reactor are identical with exemption of the angle of incidence for PARS, which have been chosen 28 deg and 30 deg for the upper and lower parts, respectively.

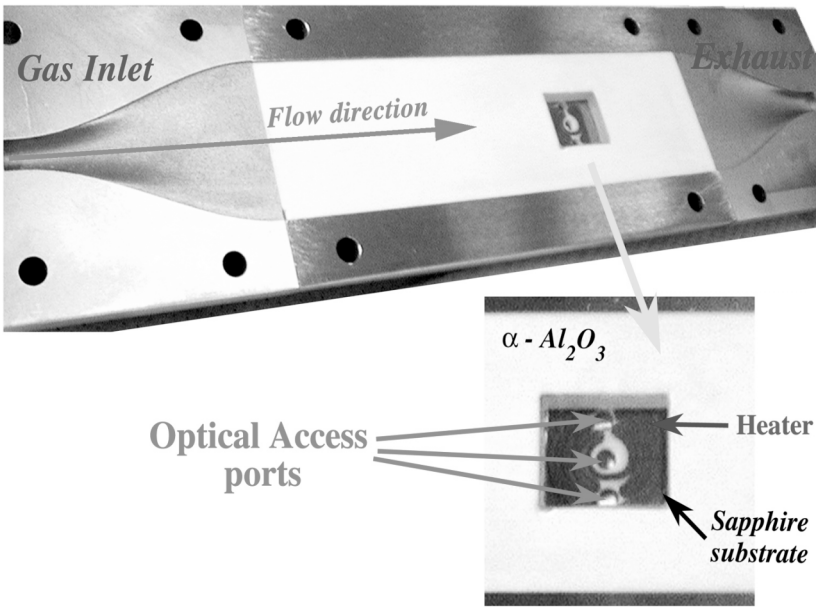

Fig. 3. Perspective view of one of the machined and assembled inner half-parts of the HPCVD reactor. The transparent Sapphire substrate allows a view on the heater element as well as to the optical ports entering from the back.

As schematically depicted in Fig.4, PARS utilizes p-polarized light impinging the substrate-ambient interface near the principal angle φ_P. The angle of total reflection, φ_T, is approximately 5 deg above φ_P. The wavelength dependency of the principal angle will shift the principal angle φ_P of more than 2 deg in the wavelength range of 200nm and 1700nm. The temperature shift is on the order of 0.2 deg between room temperature (RT) and 1000°C. Utilizing these two angles of incidence, two independent but complementary measurements can be performed at the same time. The entrance and exit ports for PARS, together with the normal incidence access port can be utilized for a variety of spectroscopic real-time techniques.

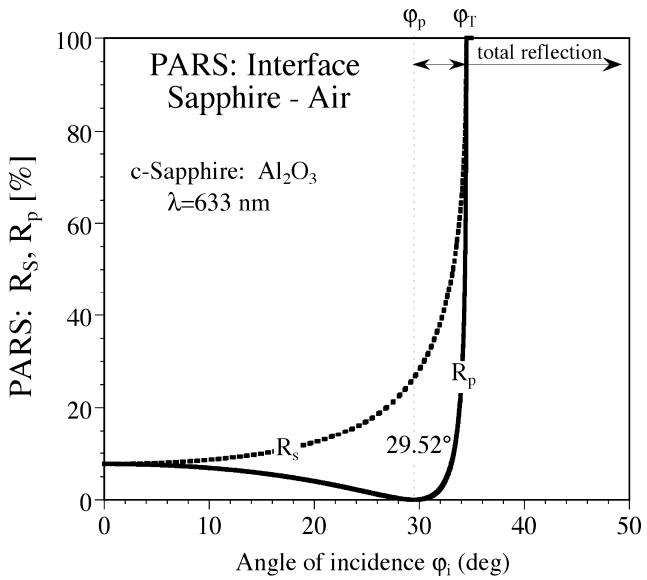

Fig. 4. Angle dependency of reflectance for p- and s- polarized light at the interface Sapphire – ambient, Depict are the characteristic angles: principal angle φ_P and total reflection angle φ_T.

3. Reactor flow characterization

Gaining an insight into the growth kinetics at elevated pressure requires an analysis of each step critical to the growth process. One crucial step is the maintenance of the laminar flow conditions in order to provide a consistent supply of precursor constituents. This allows the correlation of gas phase constituent concentrations to the diffusion processes and surface chemistry processes that drive the thin film growth process. In order to analyze the gas flow kinetics, LLS in forward geometry was applied, as schematically illustrated in the inset of Fig.5. The forward component of LLS is analyzed for laser light focused through the flow channel. Fig.5 shows the LLS intensities collected under constant pressure (9 bar) conditions and flow rates varied between 3 slm and 21 slm. The LLS intensity remains constant for flow rates below a critical point of approximately 7 slm. For flow rates above the critical point, a monotone increase in the intensity of LLS is observed. The region where the steady LLS intensity begins to increase is denoted as “transition

point*"* and indicates the transition from a laminar to turbulent flow. A slight hysteresis in the LLS intensity is observed for increasing and decreasing flow rates in the reactor. However, within the error range the "transition point" remains the same. The "transition point" is denoted as "onset of turbulent flow". The onset of increased LLS for pure nitrogen flow is summarized in Fig.6, indicating the flow and pressure regime at which laminar flow can be maintained. The associated Reynolds number can be calculated via

$$\text{Reynold's \#}\ \ Re = \frac{\rho\, u\, l}{\eta}\ , \tag{2}$$

where ρ=1.12 [kg·m^{-3}] is the density of the gas, u is the flow velocity, l is a flow parameter - a characteristic length – associated with the reactor, and η=1.12 [kg·m^{-3}·s^{-1}] is the dynamic viscosity. For ideal gases, a direct proportionality between the density of the gas, ρ, and the pressure exists. In turn, this leads to an inverse proportionality between flow velocity and pressure, when the flow parameter "l" and the dynamic viscosity, η, are constant.

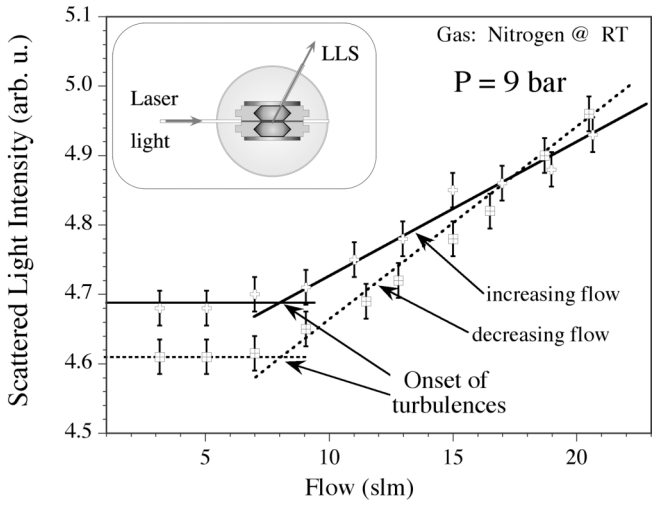

Fig. 5. Characterization of flow behavior in the HPCVD reactor. Laser light scattering (LLS) in forward geometry is used to analyze the onset of turbulence as function of pressure and flow.

The average of the calculated Reynolds number is around 1480 with no significant pressure dependency observed.[23] As shown in section V, even more detail on the flow kinetic is revealed during pulsed precursor injection studies.

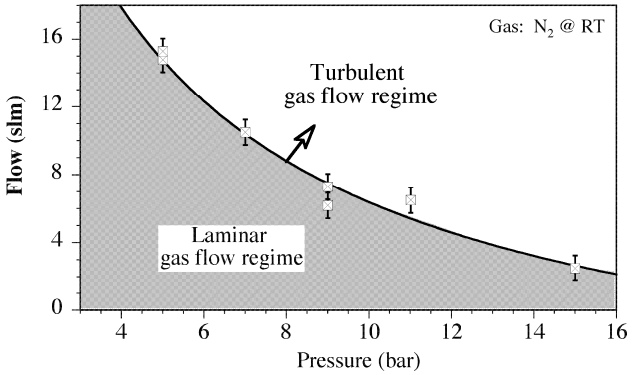

Fig. 6. Transition from laminar to turbulent flow conditions as determined by LLS intensity measurements. The inset depicts the increase of the LLS with increasing pressure.

4. Precursor characterization: Ammonia and Trimethlyindium

For above atmospheric pressures, optical diagnostic techniques are uniquely suited to provide real time information pertaining to gas flow dynamics and the gas constituents. Real-time optical diagnostics are also crucial to obtain information on the precursor flow and their decomposition kinetics. Several optical techniques have been explored, but only a small group satisfies the requirements of being robust as well as sensitive. For example, the substrate temperature during typical InN growth lies between 800K and 1200K, emitting a significant radiation as shown in Fig.7. The heater radiation intensity limits the sensitivity of many optical probe techniques in the visible and infrared (IR) regime, even if modulation techniques are applied. As depict in the inset of Fig. 7, the radiation intensity for a 1000K back body emitter below 350nm vanishes very quickly with negligible contributions below 300nm. Utilizing UVAS techniques as well as UV induced fluorescence

spectroscopy to identify the group-V and organometallic group-III precursors in the gas phase is well established in the literature.[24-27]

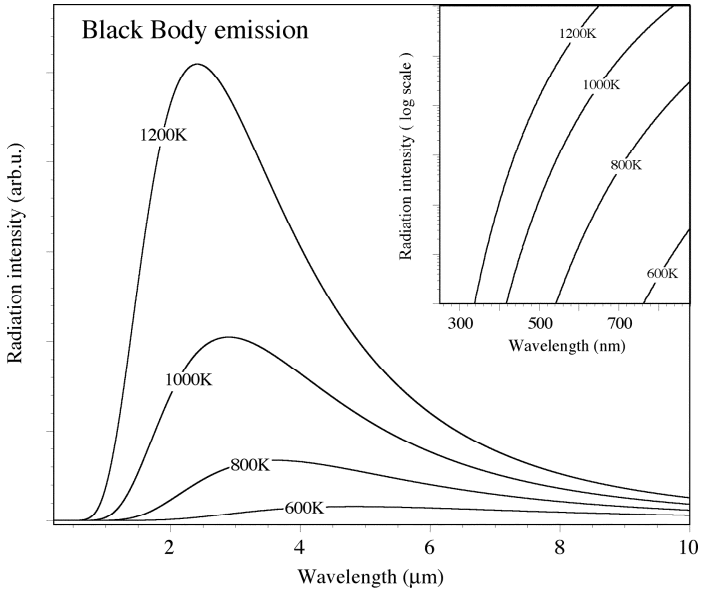

Fig. 7. Intensities and spectral distribution of a black body emitter such as a hot substrate. The inset depicted on a logarithmic scale the onset the radiation from 1200K down to 600K.

4.1. *Optical characterization of Trimethylindium, TMI, [In(CH3)3]*

A nitrogen carrier gas flow through the TMI bubbler is used to transport the TMI vapor from the bubbler to the gas control system. The molar flow of TMI directed from the bubbler in the reactor is expressed by

$$n_{TMI} = 8.3216 \cdot 10^{-9} \cdot x \quad [mol \cdot s^{-1}] \tag{3}$$

where x = (0…100% full scale [%FS]) denotes the nitrogen flow through the bubbler with 100% = 0.5 slm maximum. The molar TMI flow ratio χ through the reactor is given by

$$\chi = \frac{n_{TMI}}{n_{total}} = \frac{n_{TMI}}{n_{Main\ N_2} + n_{bubbler\ N_2} + n_{TMI}} = \frac{2.237 \cdot 10^{-5} \cdot x}{z + 10^{-2} \cdot x + 2.237 \cdot 10^{-5} \cdot x} \tag{4}$$

where z = (0…100%FS) is the main nitrogen flow with 100% = 50 slm maximum flow, which dilutes the TMI stream through the reactor.

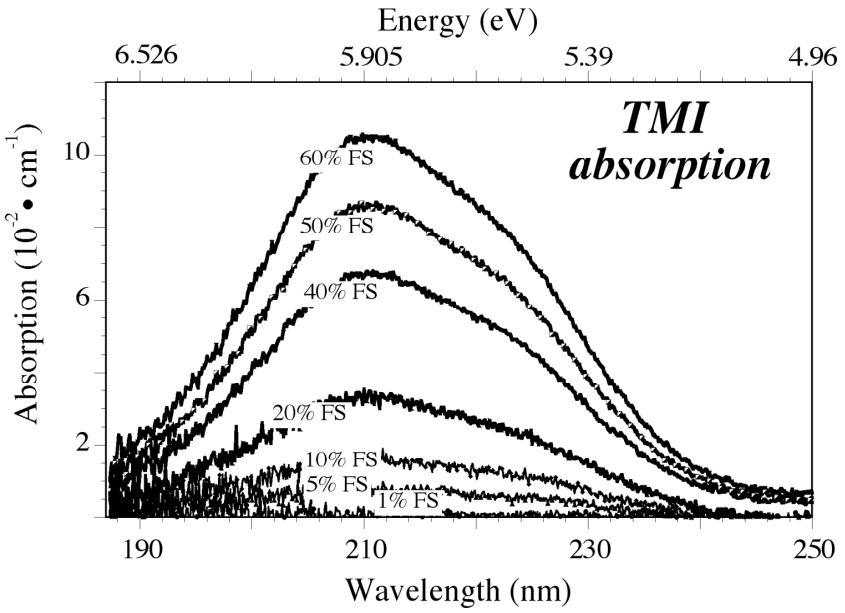

Fig. 8. Spectral resolved absorption on TMI diluted in N_2-carrier gas as function of N_2-flow through TMI bubbler in %FS. The total flow through the reactor is maintained at 5 slm at 1630 mbar.

Utilizing UVAS, the TMI induced absorption was characterized through the broad absorption band observed in the wavelength range of 190nm - 250nm with the absorption maximum centered at 210.7nm. Figure 8 shows the spectral resolved absorption structure as function of N_2-carrier flow through the TMI bubbler. For higher TMI concentrations, two absorption centers, around 210.7nm and 221nm, can be distinguished.

For higher TMI concentrations, two absorption centers, around 210.7nm and 221nm, can be distinguished. The strongest absorption maximum remains for all TMI concentrations investigated at 210.7nm, and the peak-maximum position does not change significantly with TMI concentration. The analysis of the absorption maximum at 210.7nm as a function of the molar TMI flow ratio χ shows an exponential correlation in the form of

$$\alpha(\chi) = -0.37367 + 0.37282 \cdot \mathrm{epx}\left[\frac{\chi}{5.44 \cdot 10^{-4}}\right] \quad [\mathrm{cm}^{-1}] \tag{5}$$

which allows for the calculation of the number of TMI molecules per time unit as function of the observed absorption magnitude.

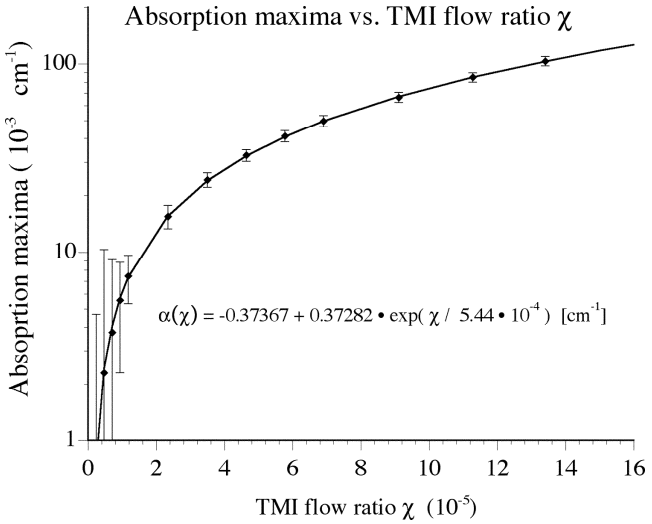

Fig. 9. Absorption strength at λ=210.7nm as function of the molar TMI flow ratio χ under steady-state flow conditions.

4.2. *Optical characterization of ammonia (NH_3)*

Near atmospheric pressures, the ammonia vapor is transported from a gas cylinder, with a pressure set at 30 psi. The NH_3 flow is controlled via a mass flow controller with a 1 slm maximum flow, expressed via y = 1 - 100%FS. The molar flow of ammonia and number of ammonia molecules per unit time are given by

$$n_{NH_3} = 7.4405 \cdot 10^{-6} \cdot y \quad [\mathrm{mol} \cdot \mathrm{s}^{-1}] \tag{6}$$

The molar ammonia flow ratio χ through the reactor, defined as the ratio of ammonia flow rate to total flow (precursor flow plus nitrogen main flow), can be expressed in term of the percentage of full scale flow, z and y as

$$\chi = \frac{n_{NH_3}}{n_{total}} = \frac{n_{NH_3}}{n_{Main\_N_2} + n_{NH_3}} = \frac{y}{50 \cdot z + y} \tag{7}$$

where z = (0…100%FS) is, again, the main nitrogen flow with 100% = 50 slm maximum flow.

The flow of ammonia through the reactor is analyzed by UVAS in the wavelength range of 180nm and 300nm as function of the molar ammonia flow through the reactor. Figure 10 shows the UV absorption spectra for ammonia flow ratios in the range of 10^{-1} to 10^{-3} at RT and a reactor pressure of 1.6 bar, which are typical molar ammonia flow ratios χ required for the growth of InN. Illustrated in Fig.10, even for the lowest flow setting, there are several of the absorption structures at higher energies that exhibit a saturation effect and are not suitable for ammonia characterization in the molar flow regime. For the ammonia flows used during the growth of InN, the UV absorption peaks centered at 217.1nm and 221.6nm are best suited. The correlation for these two absorption peak maxima with the flow ratio can be expressed as

$$\begin{aligned} \alpha_{peak\_217.1nn}(\chi) &= 0.38 \bullet \ln(\chi + 0.011) - 2.0 \bullet \chi + 1.73 \quad [cm^{-1}] \\ \alpha_{peak\_221.6nn}(\chi) &= -45 + 45.01 \bullet \exp\left(\chi / 18\right) \bullet 10^{-2} \quad [cm^{-1}] \end{aligned} \tag{8}$$

For ammonia flow ratios in the range of χ = 1.0 x 10^{-2} to 1.6 x 10^{-1}, the absorption maxima at 221.6nm is used to provide the correlation between UV absorption and the molar flow ratio χ. The number of NH_3 molecules per unit time is computed as function of the observed UV absorption. For the UV absorption feature located at 221.6nm, we find the number of NH_3 molecules per time unit as

$$N_{NH_3}(\lambda=221.6nn) = \frac{7.17 \bullet 10^{21} \bullet z \bullet \ln(\alpha')}{1 - 32 \bullet \ln(\alpha')} \quad [s^{-1}] \quad \text{with } \alpha' = \frac{\alpha_{@\ 221.6nn} - 80}{80.01} \tag{9}$$

Figure 11 shows the correlation between ammonia molecules per time unit and the ammonia flow ratio in the range of χ = 1.0 x 10^{-2} to 9.0 x 10^{-1}, for a reactor pressure of 1.6 bar. Under those conditions, the ammonia flow can be varied between 10^{19} and 2.5 x 10^{20} NH_3 molecules per sec.

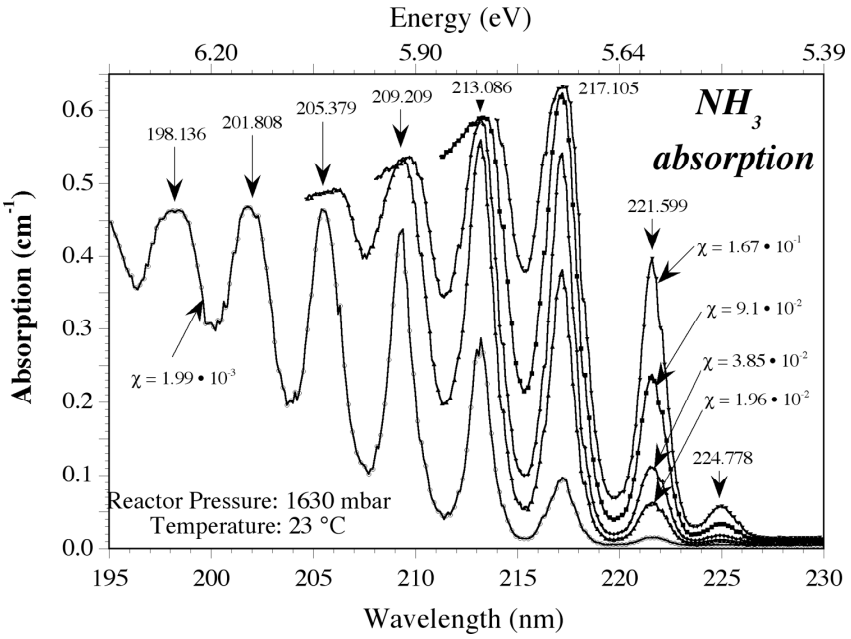

Fig. 10. Absorption spectra for various molar ammonia flow ratio χ and a rector pressure of 1.6 bar.

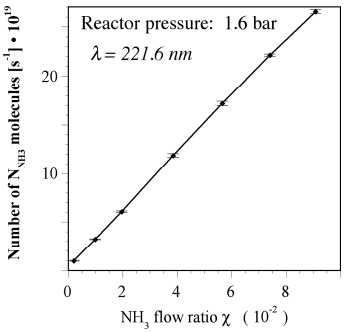

Fig. 11. Calculated concentration of ammonia molecules per sec using the absorption line at λ = 221.6nm under continuous flow conditions.

5. Flow kinetics: Analysis utilizing pulsed gas injection

The flow of the precursors at higher pressures requires a compression and dilution step in order to allow the precursors to be injected in the

HPCVD reactor. To accomplish this, a reservoir is filled at slightly above atmospheric pressure. In the following steps the reservoir is compressed with nitrogen carrier gas and temporally controlled injected into the reactor. The cycle repetition rate, duration of injection, and position of injection can the adjusted within 10ms resolution.

Figure 12 shows, as an example, typical absorption traces monitored at 210.7nm during pulsed TMI injection with a 6 sec repetition period for various reactor pressures, keeping the flow constant. The total number of TMI molecules flowing through the reactor can be calculated using the relationship between the UV absorption and TMI flow rate provided in equation 5, taking in to account the compression ratio and gas reservoir volume.

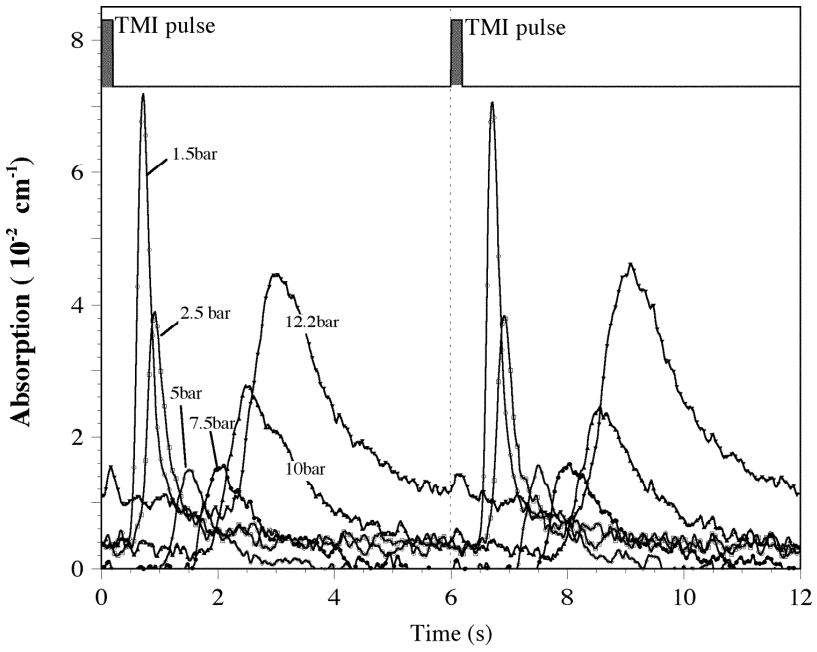

Fig. 12. Absorption traces monitored at 210.7nm during TMI precursor pulse injection in the reactor at constant flow of 5slm. The reactor pressure was varied between 1 and 12 bar. The pulse cycle sequence is 6 s with 0.2s TMI injection time.

The pulsed precursor injection has been analyzed as function of pulse width, precursor molecules per pulse, total reactor flow and reactor pressure. A carryover of the UV absorption trace from one sequence to the next is observed at reactor pressures above 10 bar. The result is an increase of the base line in the overall UV absorption. As the reactor pressure is increased for a given fix flow rate, the precursor pulses monitored at the substrate centerline show three distinct features:

(i) a systematic shift in the pulse arrival time,
(ii) a systematic TMI pulse broadening, and,
(iii) a change in the TMI absorption for pressures larger 7 bar.

5.1. *Flow characterization during pulsed precursor injection:*

The time delay, Δt, between the start of the precursor pulse injection sequence and the arrival of the diluted TMI gas at the center of the substrate is determined by the pneumatic valve opening time t_v, the reactor flow channel geometric factor r_g, the reactor pressure p_r (in bar), and the total gas flow through the reactor in terms of standard liters per min (slm). The analytic relationship is,

$$\Delta t = t_v + \frac{l_d}{v_g} = t_v + r_g \cdot \frac{p_r}{V_{slm}} \tag{10}$$

The reactor geometry factor r_g is a constant. It is functional dependent on the system parameters such as the reactor cross section A and the distance l_d between the injection valve and the substrate centerline. Its unit is $[min^{-1} \bullet bar^{-1} \bullet s^{-1}]$. The analysis of Δt for precursor pulse injection rates of 6s is shown in Fig. 13 as function of total gas flow and reactor pressure. Under these conditions, an analysis of Δt reveals that the pneumatic valve opening time $t_v = 240ms$ and the reactor geometry factor $r_g = 0.70$ can be treated as constant values. Based on the analysis the average gas velocity v_g can be computed as

$$v_g = \frac{l_{dr} \cdot V_{slm_{cor}}}{r_g \cdot p_r} = 136.7 \cdot \frac{V_{slm_{cor}}}{p_r} \quad [cm \bullet s^{-1}] \tag{11}$$

Note, that this is not the gas velocity over the substrate but rather the average velocity for the reactor system. Based on the reactor cross section A, and the gas volume per time unit, the average flow velocity over the substrate is estimated a factor 2 smaller than indicated by the average velocity v_g. This is due to the larger reactor flow channel cross section, compared to the gas lines.

The systematic precursor pulse broadening shown in Fig.12 is a direct result from the relationship between gas flow velocity and pressure given by equation 11. The reason for the pronounced increase in the TMI absorption observed for pressures larger than 6 bar is at present not fully understood and requires a more detailed study. A similar increase is observed for the ammonia precursor, for pressures above 8 bar.

The UV absorption cross-section appears to have a functional dependence on pressure since at high pressures the UV absorption in noticeably increased. Such an increase would be beneficial for the decomposition kinetics of the precursors since it would result in a more efficient decomposition of the precursors. However, detailed theoretical calculations will be required and be validated by experimental real-time measurements.

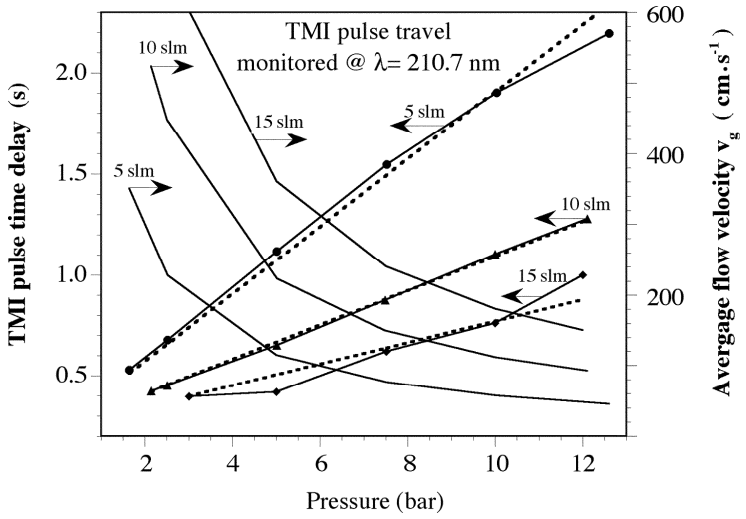

Fig. 13. Time shift between injection and onset of pulse arrival at the substrate centerline as function of the reactor pressure and for different flow rates. The right scale

shows the computed average gas velocity v_g between the TMI reservoir and the substrate center line.

As shown above, the real-time optical analysis of pulsed precursor injection, provides crucial information pertaining to

- the reactor flow characteristics and average gas flow velocity,
- pulse broadening, and
- pressure related changes in the optical properties of the precursors.

What is most important, however, is that these features provide a pathway for the monitoring and engineering of the gas phase chemistry and surface chemistry by enabling precise engineering of precursor pulse separation and/or overlap. Such knowledge and capabilities are crucial for a more physically realistic and accurate modeling effort and for more precise control of the growth process at high-pressures.

6. Precursor decomposition dynamics at higher pressures

The analysis of the decomposition dynamics of ammonia under continuous ammonia flow conditions and slightly above atmospheric pressures was done with the aid of UVAS.[28] However, at higher reactor pressures, a continuous precursor decomposition analysis is no longer possible. A periodic pulse injection scheme is used in which the average absorption peak maxima are analyzed as a function of precursor concentration and temperature. Figure 14 shows the temperature dependency of the UV absorption of ammonia monitored at 210.7nm while maintaining a reactor pressure of 10 bar.

For this elevated pressure, the onset of decomposition as indicated by a decrease in the UV absorption occurs at a temperature of about 850K. Compared to studies at atmospheric pressures, where the ammonia decomposition is observed at about 900K, this is a significant reduction in the decomposition temperature. As for ammonia, we also analyzed the TMI UV absorption peak maxima at 213nm during pulsed precursor injection as a function of pressure and temperature. At present, we a not aware of any experimental studies on the decomposition dynamics of TMI at higher pressures. Figure 15 shows the TMI peak absorption data for a reactor pressure of 10 bar as function of temperature. The analysis

indicates that the onset of decomposition in the gas phase occurs around 800K.

This onset in decomposition is slightly higher than those reported under low-pressure OMCVD conditions.[25,29] More detailed studies using UVAS and optical emission spectroscopy as function of pressure are required to correlate the experimental results to theoretical predications for the TMI decomposition at elevated pressures as formulated by Cardelino et.al.[30]

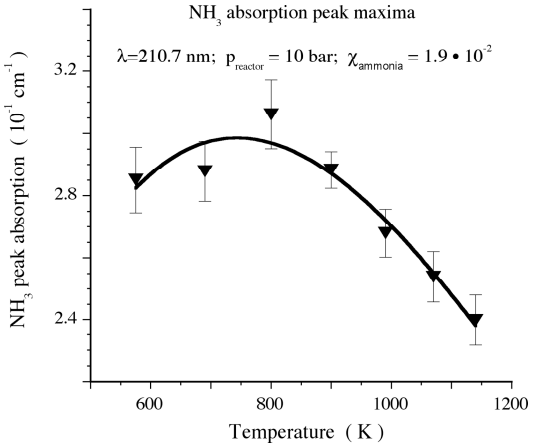

Fig. 14. Change of the ammonia absorption peak maximum as function of temperature.

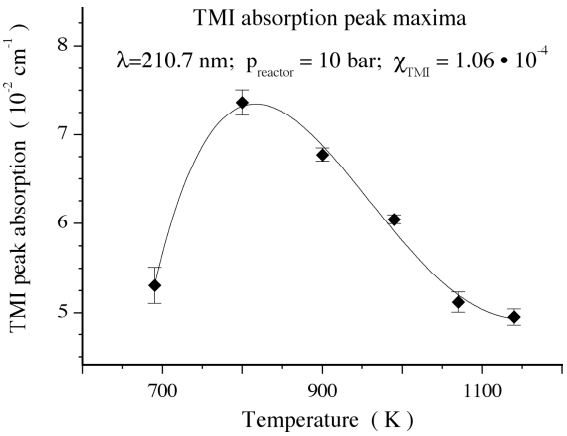

Fig. 15. Decomposition of TMI at 10 bar reactor pressure, monitored during pulsed TMI injection as function of temperature.

The observed decrease of the temperature at which the onset of ammonia decomposition occurs under elevated pressure conditions is crucial for the optimization of the growth of InN and the control of point defect chemistry in this material system.

7. Growth of InN: Real-time optical monitoring

The decomposition studies for ammonia in the previous section suggests that for sufficient cracking of the ammonia precursor growth temperatures of above 1000K to be used. However, literature data for InN growth by OMCVD indicate a growth temperature of 675K to 750K,[7] 775K,[31] 810K - 840K.[32] Under HPCVD conditions the growth temperatures can be increased significantly as shown below. Reported NH_3:TMI flow ratios under low-pressure OMCVD conditions vary from 10^3 to 10^4 in order to counteract the low ammonia decomposition at the growth temperatures.[7,31]

The growth by HPCVD has to address the *control of gas phase reactions and the effective diffusion of the nutrients to the growth surface.* These considerations lead to the concept of a pulsed injection scheme as schematically shown in Fig.16. The TMI and NH_3 precursors are temporally controlled and embedded in a high pressure carrier stream, consisting of ultra-pure nitrogen, supplied from a boil-off liquid nitrogen tank. The total gas flow as well as the reactor pressure are kept constant at all times.

The repetition rate "*cycle sequence*" as well as the precursor pulse length and position within the *cycle sequence* are crucial growth control parameter that allow the precise engineering of gas phase and surface chemistry processes during the nucleation phase and during steady-state growth conditions. For the InN layers discussed in more detail below, the cycle sequence time was varied from 4 sec to 10 sec, with TMI and ammonia pulse widths from 0.3-0.6sec and 0.8-1.5 sec, respectively. The pulse separation was varied from 1 to 5 sec.

A typical growth procedure contains the following steps. The symmetrically embedded substrates in the upper and lower part of the reactor are heated to approximate 1150K - 1200K and exposed to ammonia for typically 30 min. Prior to the growth, the temperature is

lowered to the growth temperature, and the InN growth is initiated by supplying the precursors sequentially as shown in Fig.16.

The integrated optical access ports along the center axis of the substrates are used to monitor the gas constituents by UVAS, as described in section IV and V.

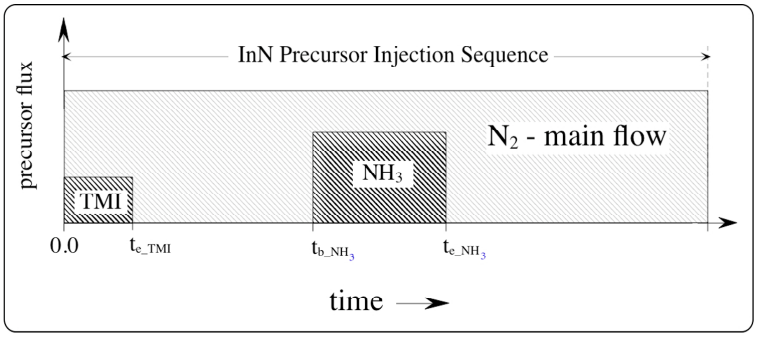

Fig. 16. Schematic representation of a precursor cycle sequence used for the growth of InN via the precursors TMI and ammonia.

The growth surface conditions are monitored through the backside of the sapphire substrate using PAR and LLS.[19,22,23] For the growth results presented here, the reactor pressures were kept around 10 bar and a total carrier flow rate in the range 2 slm to 12 slm. The precursor flow was evaluated for molar ratio ammonia to TMI, $R_{NH3:TMI}$, from 100 to 5000. The growth temperature has been varied from 800K to 1150K. Note that all temperatures settings refer to a calibrated correlation curve between the measured black body radiation distribution as function of "heater" power setting. Keep in mind, that the actual gas phase temperatures and the growth surface temperatures are strongly influenced by the gas flow velocity (total main flow) and surface emissivity. Specifically, the surface emissivity changes during growth, which affects the actual growth temperature. The temperature referred to is not corrected for these effects.

A typical set of real-time optical monitoring traces by PAR and LLS is illustrated in Fig.17. The temporal evolution of the PAR trace contains crucial information related to the growth surface as well as to the growth

history. The developing PAR interference fringe provides information on the overall layer growth (*history*), while the superimposed '*fine structure*' on the PAR interference fringe (not resolved in Fig.17) provides insights on the growth surface chemistry and kinetics (see below). The monitored LLS trace tracks the evolution of the surface morphology, providing details on the nucleation and overgrowth kinetics as well as the overall surface roughness. As shown in Fig.17, the LLS signal increases during the film nucleation phase, but it decreases during the further steady-state growth. The ex-situ inspection revealed a mirror-smooth surface.

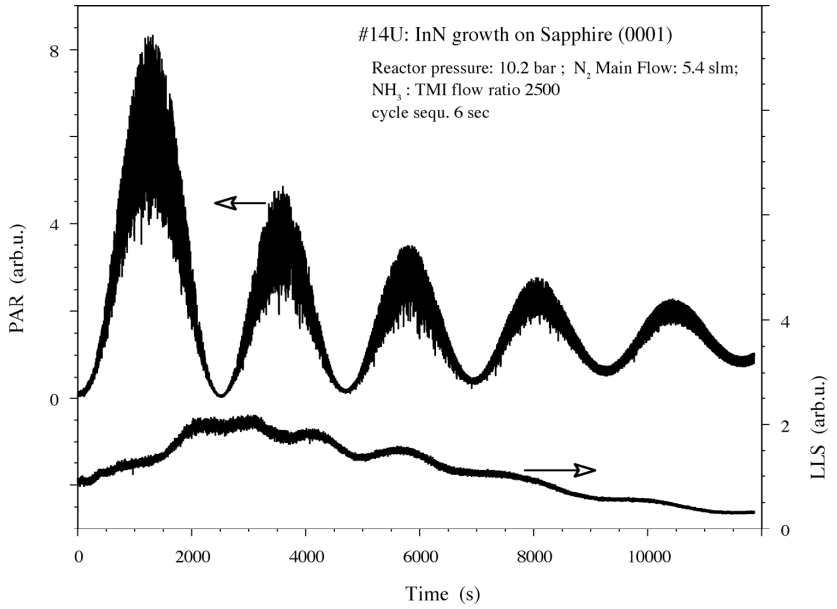

Fig. 17. Real-time optical monitoring of InN growth by PAR and LLS..

From the analysis of the PAR signal, the average growth rate and the difference between the dielectric functions of film and substrate can be estimated. The analysis of In#14u provided the average growth rate as 1.346Å per cycle sequence. By varying the TMI and ammonia concentration per injection pulse, the growth rate per cycle sequence can be adjusted from a fraction of a monolayer (ML) to 1ML and beyond per

cycle sequence. This capability allows the precise engineered growth of nano-structured composites with sub-monolayer resolution.

A more detailed insight in the growth process is gained by analyzing the PAR *fine structure* and by linking it to the UV absorption traces, which monitors the gas phase constituents. As an example, Fig. 18 shows the observed PAR and UV absorption traces during the nucleation phase and steady-state growth of InN. The lower half in Fig.18a shows the UV absorption trace recorded for the wavelength λ=210.8nm, monitoring the un-decomposed ammonia and TMI species above the growth surface. The PAR trace in the upper half of the figure is recorded for the wavelength λ=632.8nm, monitoring highly sensitive changes in the dielectric function at the substrate-ambient interface. Also indicated in the figure are the positions of the precursor pulse injections with a total cycle sequence repetition time of 6 sec.

First, note that the precursor injection time and the response seen in UVAS and PAR are temporally shifted, which is due to the average travel time of the precursors between valve and substrate center line (see section V). Secondly note, it takes about two cycle sequences before the UV absorption feature for TMI clearly develop (see arrows). Looking at the PAR response, a large increase is observed after the first TMI - ammonia combination is introduced, indicating the start of InN nucleation and the presence of TMI fragments in the vicinity of the growth surface.

A steady state surface chemistry is typically reached after 5 to 20 cyclic precursor exposures, depending on substrate temperature, precursor flow ratio, gas phase velocity and reactor pressure. Figure 18b shows the PAR and UVAS responses during steady-state growth conditions. The periodic modulation of the PAR response can be directly correlated to the presence of ammonia and TMI fragments in a surface reaction layer and at the growth surface. The overall decrease in the PAR signal is correlated to the InN growth per cycle sequence as discussed in detail for p-polarized reflectance.[22,33]

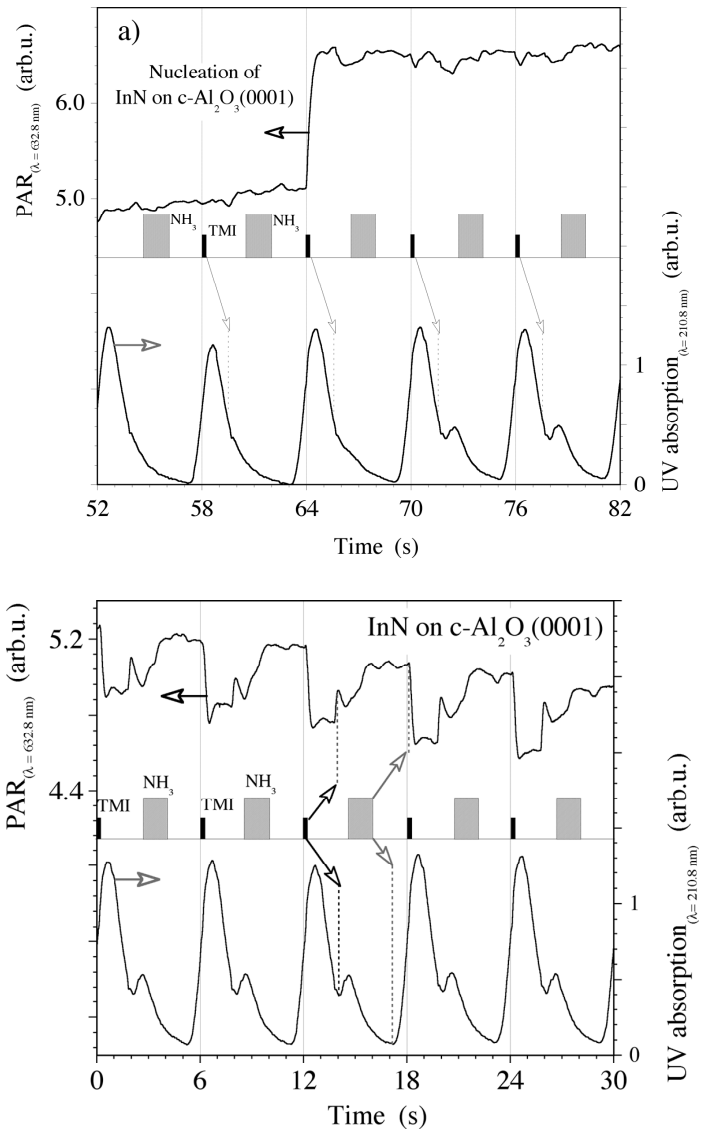

Fig. 18. (a) Monitoring of InN nucleation by PAR and UV absorption traces. A precursor cycle sequence of 6 sec with 0.4 sec TMI and 1.4 sec ammonia pulses, separated by 1.4 sec were used. (b) PAR and UV absorption traces during steady-state InN growth at 990K. The rector pressure was 10 bar with a total flow of 5 slm. The overall decrease in the PAR signal corresponds to InN growth.

At present, only the UV absorption features of TMI are monitored and related to the PAR response. The optical access ports in the HPCVD reactor enable the use UV absorption spectroscopy,[26] fluorescence,[25] and Raman spectroscopy[34] to monitor the decomposition process and the concentration of the TMI fragments. Such detailed knowledge will provide the base for a more comprehensive growth modeling that will link the growth process and flow kinetic models to surface chemistry models and the thin film growth process itself.

8. Ex-situ characterization of InN layers

The structural properties of epitaxially grown InN films have been investigated using X-ray diffraction, Auger Electron Spectroscopy (AES), and Raman spectroscopy. Figure 19 depicts the XRD pattern recorded in the ω-2θ mode for sample #C, showing single phase InN diffraction peak at 31.265, due to the (0002) reflection from wurtzite-type InN with full-width at half-maximum (FWHM) on the order of 800 arcsec.

The compositional analysis by AES (including depth profile analysis) shows indium and nitrogen as the main constituents. The AES analysis of earlier samples indicated oxygen and carbon contaminations of up to one percent. The installation of an in-line oxygen purifier reduced the oxygen concentrations below the detection limits, confirming that the oxygen contamination correlates to the residual water content in the ammonia source. No oxygen contamination was found in the main carrier gas, for which ultra-pure nitrogen (boil-off from liquid nitrogen tanks) is used. For the samples discuss below, no correlation of oxygen content with the absorption edge shift was found, confirming studies by Butcher et al.[11] indicating that the incorporation of oxygen does not directly correlate to changes in the lattice constant.

The observed carbon contamination was found to scale with the flow velocity and growth temperature. For a constant substrate temperature and estimated gas flow velocities below 40cm•s^{-1}, visible carbon precipitations are observed towards the end substrate. Increasing the gas flow velocity to 45cm•s^{-1} and above resulted in uniform InN layers. Note, even though the substrate temperature was kept constant, an increase in

the gas flow velocity will not only lead to an effective lower gas phase temperature, but will also effect the diffusion rate of the precursor constituents to the growth surface. More experimental studies are needed to link the observed data to a comprehensive model that combines gas flow kinetics, gas phase chemistry, and diffusion processes to the surface growth dynamics. The carbon incorporation in the layers and its effect on the material defect chemistry will be he most challenging part in the material optimization.

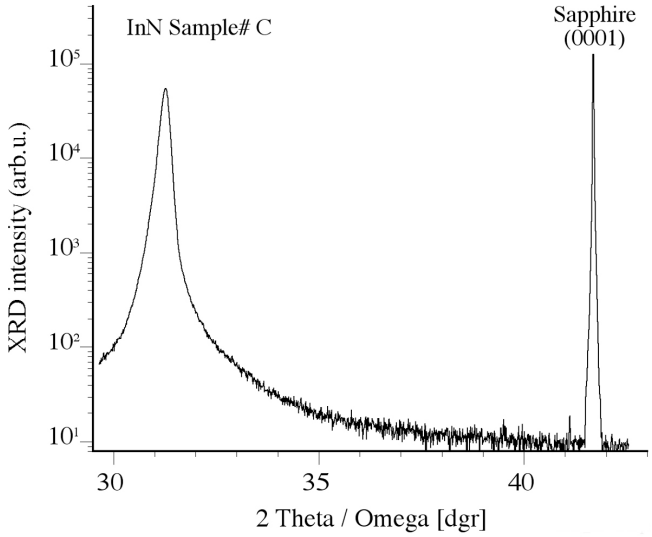

Fig. 19. XRD spectra from InN layers grown on sapphire (0001) with an ammonia to TMI flow ratio of 1000.

Raman spectroscopy has been applied as a routine technique in order to evaluate the crystallinity of the layers. The Raman spectra were measured at room temperatures in a backscattering geometry with an excitation energy of 2.33eV. Here we focus on the analysis of five representative InN samples labeled sample #A through #E. The samples were grown at temperatures around 1100K, with molar ratio ammonia to TMI, $R_{NH3:TMI}$, of 200 and 1000. All samples are typically 500nm to 800nm thick. Figure 19 shows the Raman spectra of these five samples, together with the Raman spectrum of the sapphire (0001) substrate. Sample #A and #B were grown with $R_{NH3:TMI}$ = 1000, while for the

samples #C , #D and #E, the ammonia to TMI ratio has been subsequent lowered to approximate 200.

The Raman spectra of samples #A and #B show a broad asymmetric structure that can be fitted by three Lorentzian distribution functions located approximately at 580cm^{-1}, 540cm^{-1}, and 470cm^{-1}. For samples #C through #E, the broad asymmetric structure breaks in at least 5 structures with significant variations in their peak intensities and FWHM. The polarization-dependent Raman studies on these samples remain to be performed.

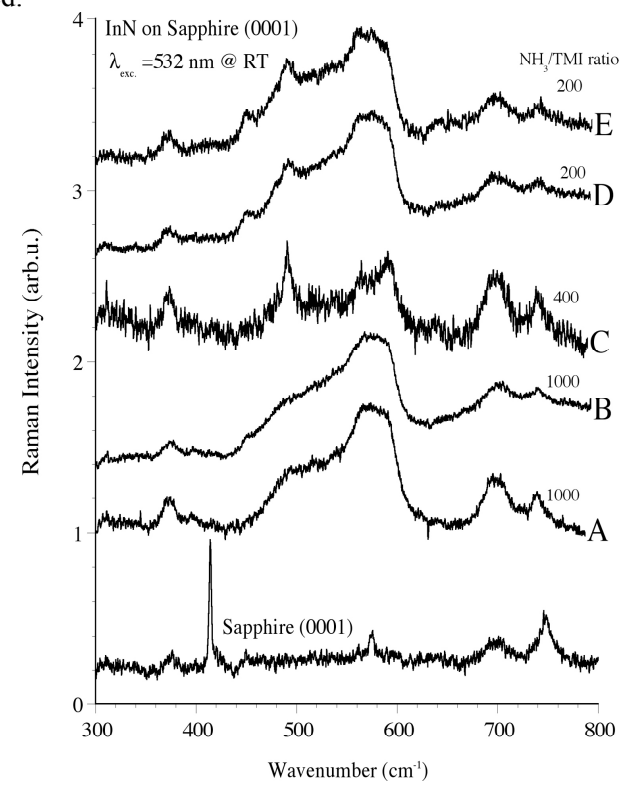

Fig. 20. Raman spectra for InN sample# A through #E. The layers were deposited around 1100K with varying the ammonia to TMI ratio.

Following the notation and peak assignment nomenclature provided by V. Davydov et.al.[2] and considering the modes of symmetry that are Raman active, the high-resolution Raman spectra for samples #E and #D

in the range of 420cm^{-1} and 620cm^{-1} were fitting by five Lorentzian distribution functions as depicted in Fig. 21.

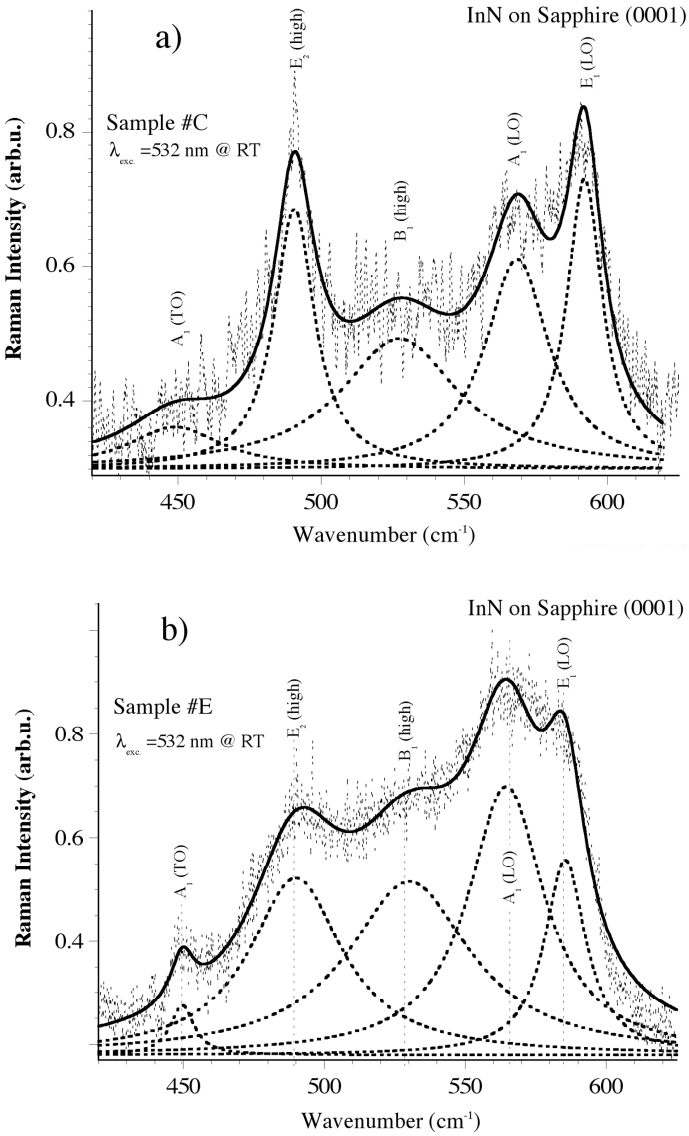

Fig. 21. Analysis of Raman modes for (a) sample# C and (b) sample #E (see text).

The analysis of the peak-positions and FWHM are summarized in Table 1, together with literature values. The most pronounced difference in the spectra of samples #C and #D is the significant increase of the A1(LO) and A1(TO) peak intensities in sample #D.

Table 1: Frequencies and FWHM of Raman peaks in samples #C and #D

Sample #	A_1(TO)	E_1(TO)	E_2(high)	B_1(high)	A_1(LO)	E_1(LO)
#C: Pos.	449 cm^{-1}	--	490 cm^{-1}	525 cm^{-1}	567.4 cm^{-1}	591 cm^{-1}
FWHM	40 cm^{-1}		17 cm^{-1}	50 cm^{-1}	13 cm^{-1}	15 cm^{-1}
#D: Pos.	451cm^{-1}	--	488 m^{-1}	528 m^{-1}	565.3 m^{-1}	588 m^{-1}
FWHM	8.9 cm^{-1}		35 cm^{-1}	61 cm^{-1}	40 cm^{-1}	26.6 cm^{-1}
Ref. 2, 35	447	475	488	565	586	593

In order to correlate the structural properties, analyzed by Raman spectroscopy, to the optical properties, absorption and reflectance spectroscopy have been applied. The absorption spectra for the five samples were taken in the spectral range of 350nm to 2300nm, the results of which are summarized in Fig.22. All samples show a pronounced absorption peak, centered at 0.63eV. Starting with sample #A, three additional absorption peaks at 0.87eV, 1.35eV and 1.8eV (shoulder) are observed. In samples #B and #C, the absorption peaks at 0.87eV and 1.35eV are increased in intensity but still visible as absorption centers. The spectrum for #C suggest already an overall shifted absorption edge and it also indicate a new (or shifted) absorption structure at 1eV. The absorption peaks at 0.63eV and 0.87eV seem have merged for sample #C. The absorption spectrum for sample #D shows a further increase in the absorption intensity for the absorption center at 1.35eV, shifting the absorption edge further down below 1eV. The absorption spectrum for sample #E indicate an absorption edge below 0.63eV.

The development of the absorption structures for these five samples suggest that the observed absorption edge shift from 1.85eV down to below 0.63eV is caused by a series of absorption structures, centered around 1.6eV, 1.35eV, 1eV, 0.87eV and 0.63eV. The appearance and

strength of these absorption centers correlate / coincide with the strength and FWHM of the Raman modes shown in Fig.20 and 21. They also correlate with the reduction of the molar ammonia to TMI precursor flow ratio, suggesting a close correlation between precursor ratio and the stoichiometry of the deposited layers. These initial results demonstrate that the precise control of the indium to nitrogen ratio is of crucial importance for optimizing the InN layer quality and with it the optoelectronic properties in this material system.

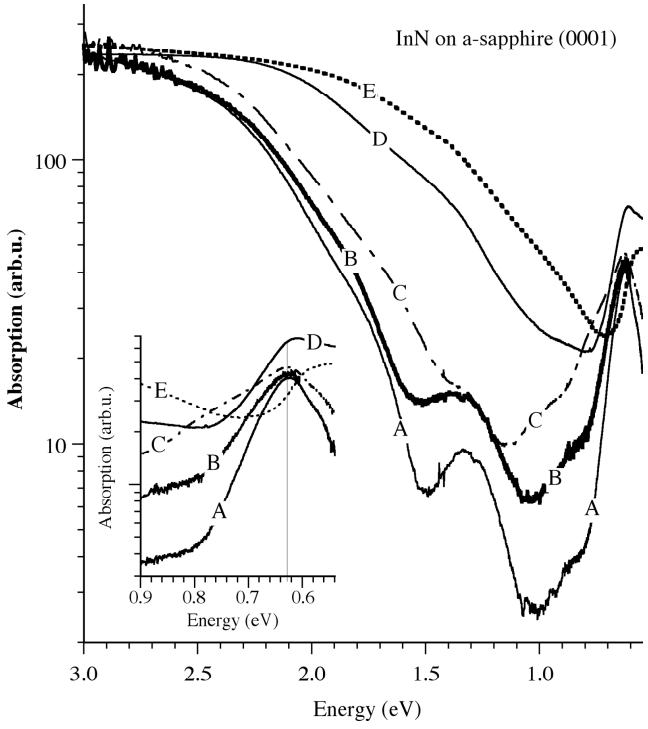

Fig. 22. Absorption spectra for various InN layers grown at 12 bar and 1100K. The gas flow velocity over the growth substrates and the molar ratio of ammonia to TMI was varied (see text).

9. Summary and Outlook

High-pressure chemical vapor deposition has been introduced for the growth of InN and related materials and shown to be a valuable method

for achieving this goal. The growth of InN has been accessed in the pressure range of 10 to 15 bars for various gas flow velocities and molar ammonia to TMI ratios. High quality InN layers were achieved for growth temperatures in the range of 1000K to 1150K with the potential of even higher substrate temperatures at higher reactor pressures. Real-time optical growth characterization by UVAS, PAR and LLS has been applied, providing critical insights in the gas phase decomposition kinetics, surface chemistry processes during the film growth process. The high sensitivity of PAR in combination with UVAS will allow to formulate a comprehensive gas flow and surface chemistry model which will enable growth control with sub-monolayer resolution.

The optical InN layer characterization results show that the shift of the absorption edge form 1.85eV down to below 0.63eV is caused by the appearance of several absorption centers as the crystallinity of the InN lattice improves. At present, the origin of these absorption centers is not clear. However, they are clearly linked to the indium and nitrogen point defect chemistry. The initial results suggest that the molar ammonia to TMI flow ratio under HPCVD conditions is below 200 due to the efficient cracking of the nitrogen precursor at the high growth temperature. Further studies varying the ammonia to TMI flow ratio, the center flow velocity, and the growth temperatures will be needed to access the optimum growth window. A further increase in the reactor pressure may allow even higher growth temperatures, bringing it closer the optimum growth temperature of GaN. This will allow for the exploration of indium rich $In_{1-x}Ga_xN$ and $In_{1-x}Al_xN$ alloys and heterostructures.

Acknowledgments

This work was supported by NASA grant NAG8-1686 and GSU-RPE.

References

1. A. G. Bhuiyan, A. Hashimoto, and A. Yamamoto, *J. Appl. Phys*. **94**, 2779 (2003).
2. V. Yu. Davydov and A. A. Klochikhin, *Semiconductors* **38**, 861 (2004).
3. T. Inushima, V. V. Mamutin, V. A. Vekshin, S. V. Ivanov, T. Sakon, M. Motokawa, and S. Ohoya, *J. Crystal Growth* **227-228**, 481 (2001).

4. J. Wu, W. Walukiewicz, W. Shan, K. M. Yu, J. W. Ager III, E. E. Haller, Hai Lu, and William J. Schaff, *Phys. Rev. B* **66**, 201403 (2002).
5. R. A. Oliver, C. Nörenberg, M. G. Martin, M. R. Castell, L. Allers and G. A. D. Briggs, *Surface Science* **532-535**, 806 (2003).
6. J. Aderhold, V. Yu. Davydov, F. Fedler, H. Klausing, D. Mistele, T. Rotter, O. Semchinova, J. Stemmer and J. Graul, *J. Crystal Growth* **222**, 701(2001).
7. Bi Z.X. Bi, R. Zhang, Z.L. Xie, X.Q. Xiu, Y.D. Ye, B. Liu, S.L. Gu, B. Shen, Y. Shi and Y.D. Zheng, *Mat. Lett.* **58**, 3641 (2004).
8. J. Wu, W. Walukiewicz, K. M. Yu, J.W. A.III, E. E. Haller, H. Lu, W.J. Schaff, Y. Saito, and Y. Nanishi", *Appl. Phys. Lett.* **80**, 3967 (2002).
9. I. Vurgaftman and J.R. Meyer, *J. Appl. Phys.* **94**, 3675 (2003).
10. E. Kurimoto, M. Hangyo, H. Harima, M. Yoshimoto, T. Yamaguchi, T. Araki, Y. Nanishi, K. Kisoda , *Appl. Phys. Lett*. **84**, 212 (2004).
11. K. S. A. Butcher, M. Wintrebert-Fouquet, P. P.-T. Chen, T. L. Tansley, H. Dou, S. K. Shrestha, H. Timmers, M. Kuball, K. E. Prince, and J. E. Bradby, *J. Appl. Phys*. **95**, 6124 (2004).
12. V. Yu. Davydov, A. A. Klochikhin, V. V. Emtsev, A. V. Sakharov, S. V. Ivanov, V. A. Vekshin, F. Bechstedt, J. Furthmüller, J. Aderhold, J Graul, A. V. Mudryi, H. Harima, A. Hashimoto, A. Yamamoto, J. Wu, H. Feick and E. E. Haller, *Proc. SPIE* **5023**, 68 (2003).
13. V.Yu. Davydov, A.A. Klochikhin, V.V. Emtsev, D.A. Kurdyukov, S.V. Ivanov, V.A. Vekshin, F. Bechstedt, J. Furthmüller, J. Aderhold, J. Graul, A.V. Mudryi, H. Harima, A. Hashimoto, A. Yamamoto, E.E. Haller, *Physica Status Solidi B*, **234**, 787 (2002).
14. F.-H. Yang, J.-S. Hwang, K.-H. Chen, Y.-J.Yang, T.-H. Lee, L.-G. Hwa and L.-C. Chen, *Thin Solid Films* **405**(1-2), pp. 194-197 (2002).
15. V. Ya. Malakhov, *Solar Energy Materials and Solar Cells*, **76**, 637 (2003).
16. B. Onderka, J. Unland, R. Schmid-Fetzer, *J. Mater. Res.* **17**, 3065-3083 (2002).
17. J. MacChesney, P.M. Bridenbaugh, and P.B. O'Connor, *Mater. Res. Bull.* **5**, 783 (1970).
18. B. H. Cardelino, C. E. Moore, C. A. Cardelino, D. O. Frazier, K. J. Bachmann, *J. Phys. Chem. A* **105**, 849 (2001).
19. N. Dietz, S. McCall, K.J. Bachmann, *Proc. Microgravity Conf. 2000*, NASA/CP-2001-210827, pp. 176 -181 (2001).
20. N. Dietz, V. Woods, S. McCall and K.J. Bachmann, *Proc. Microgravity Conf. 2002*, NASA/CP-2003-212339, pp. 169 -181 (2003).
21. N. Dietz, H. Born, M. Strassburg and V. Woods, *Mat. Res. Soc. Symp. Proc.* **798**, Y10.45.1 (2004).
22. N. Dietz, "Real-time optical Characterization of thin film growth," *Mat. Sci. & Eng. B* **87**(1), pp.1 - 22 (2001).

23. V. Woods, J. Senawirante, and N. Dietz, *J. Vac. Sci. Technol. B* **23**(4), pp. 1790-1794 (2005).
24. G. A. Hebner, K. P. Killeen and R. M. Biefeld, *J. Crystal Growth,* **98**(3) pp. 293-301 (1989).
25. G. A. Hebner and K. P. Killeen, *J. Appl. Phys.* **67**(3) pp. 1598-1600 (1990).
26. H. Okabe, M. K. Emadi-Babaki and V. R. McCrary, *J. Appl. Phys.* **69**(3), 1730-1735 (1991)..
27. M. C. Johnson, K. Poochinda, N. L. Ricker, J. W. Rogers Jr. and T. P. Pearsall, *J. Cryst. Growth* **212**, 11 (2000).
28. N. Dietz, M. Strassburg and V. Woods, *J. Vac. Sci. Technol. A* **23**(4), pp. 1221-1227 (2005).
29. J. Haigh and S. O'Brien, *J. Crystal Growth* **68**, 550 (1984).
30. B. H. Cardelino, C. E. Moore, C. A. Cardelino, S. D. McCall, D. O. Frazier, K. J. Bachmann; *J. Physical Chemistry A*, **107**, 3708 (2003).
31. T. Schmidtling, M. Drago, U. W. Pohl and W. Richter, *J. Crystal Growth* **248**, 523 (2003).
32. A. Jain, S. Raghavan and J. M. Redwing, *J. Crystal Growth* **269**, 128 (2004).
33. N. Dietz and K. J. Bachmann, *Vacuum* **47**, 133 (1996).
34. C.Park,W.-S. Jung, Z. Huang and T. J. Anderson, *J. Mater. Chem.* **12**, pp. 356–360 (2002).
35. V. Y. Davydov, V. V. Emtsev, I. N. Goncharuk, A. N. Smirnov, V. D. Petrikov, V. V. Mamutin, V. A. Vekshin, S. V. Ivanov, M. B. Smirnov and T. Inushima, *Appl. Phys. Lett.* **75**, 3297 (1999).